

# Comparative analysis of the plasma parameters of ECR and combined ECR+RF discharges in the TOMAS plasma facility

**Yu Kovtun<sup>1</sup>, T Wauters<sup>2</sup>, A Gorjaev<sup>2,7</sup>, S Möller<sup>4</sup>, D López-Rodríguez<sup>2</sup>, K Crombé<sup>2,7</sup>, S Brezinsek<sup>4</sup>, A Dinklage<sup>5</sup>, D Nicolai<sup>4</sup>, Ch Linsmeier<sup>4</sup>, M Van Schoor<sup>2</sup>, J Buermans<sup>2,7</sup>, S Moon<sup>6</sup>, R Ragona<sup>2</sup>, P Petersson<sup>6</sup>**

<sup>1</sup> Institute of Plasma Physics, National Science Center ‘Kharkov Institute of Physics and Technology’, Kharkiv, Ukraine

<sup>2</sup> Laboratory for Plasma Physics, LPP-ERM/KMS, B-1000 Brussels, Belgium

<sup>4</sup> Institute for Energy and Climate Research – Plasma Physics, Forschungszentrum Jülich GmbH, Jülich, Germany

<sup>5</sup> Max-Planck-Institute for Plasma Physics, Greifswald, Germany

<sup>6</sup> KTH Royal Institute of Technology, Stockholm, Sweden

<sup>7</sup> Department of Applied Physics, Ghent University, 9000 Ghent, Belgium

E-mail: Ykovtun@kipt.kharkov.ua

## Abstract

The TOMAS toroidal magnetized plasma facility aims at complementary research on wall conditioning methods, plasma production and plasma-surface interaction studies. This paper explores for the first time the parameters in helium ECR plasma and combined ECR+RF discharges in TOMAS. The ECR discharge in this work, at 2.45GHz and 87.6mT, is the main one for creating and maintaining the plasma, while the addition of RF power at 25MHz allows to broaden the achievable electron temperature and density at a given gas flow, as evidenced by triple Langmuir probe measurements. This effect of the combined ECR + RF discharge provides flexibility to study particular aspects of wall conditioning techniques relevant to larger devices, or to approach plasma conditions relevant to fusion edge plasmas for particular surface interaction studies.

Keywords: ECR, RF, magnetized discharge, triple probe, TOMAS

---

## 1. Introduction

High-frequency discharges of various frequency ranges between 1 MHz and 300 GHz are widely used in physics research and applied plasma process technologies [1-7]. This includes generation and heating of high-temperature plasma in devices for controlled thermonuclear fusion where one distinguishes the MHz and GHz range, respectively, as the ion and electron cyclotron range of frequency [8-11]. In plasma process technologies based on radio-frequency (RF) discharges, the most often used generator frequency is

13.56 MHz, producing a low-temperature plasma for various applications [2-5]. These RF discharges can be performed both with and without magnetic field. In thermonuclear research, the RF frequency is usually set as a multiple (harmonics) of the ion cyclotron (IC) frequency [11]. The main feature of IC discharges is the ability to heat the ionic component of the plasma which is advantageous to reach fusion conditions. IC-based methods are also used for cleaning vacuum chambers [12-14]. In weak magnetic fields, RF discharges are used for cleaning at frequencies above the IC frequency [15-17].

Microwave discharges in a magnetic field at frequencies (0.915 – 200 GHz) which are multiples of the electron-cyclotron frequency (ECR) have become widespread [1-3, 6-10]. Plasma sources based on ECR are used for various types of surface treatment, etching, deposition of thin films, sources for powerful ion beams, electric propulsion etc. [1, 2, 7]. Microwave plasma sources mainly use the frequency of 2.45 GHz. In fusion research, ECR discharges are used to create and heat plasma [8-10]. The feature of ECR discharges is the ability to heat the electron component of the plasma. The applied generator frequency in such studies depends on the magnitude of the magnetic field attainable in the installations. For example, in the Wendelstein 7-X stellarator gyrotrons are set up at a frequency of 140 GHz [10]. ECR discharges are also applied for wall conditioning of toroidal vacuum chambers of tokamaks and stellarators [12, 14] employing the same generators and magnetic fields as those for plasma generation and heating [18, 19]. Wall conditioning modes at a frequency of 2.45 GHz in weak magnetic fields have become widespread [12, 20].

Both IC and ECR have been applied for cleaning vacuum chambers of fusion devices [12-14]. Also combined ECR + RF discharges were investigated for various plasma process technologies [21-24]. Typically, these discharges use a substrate (used for technological purposes, for example, etching etc.) as an electrode. The electrode is biased by the RF power source relative to the chamber wall. In this case, the scheme of plasma sources is similar to inductively coupled plasma reactors [4]. But instead of an inductive discharge, an ECR discharge is used. A combination of ECR and IC discharge was used to condition the walls of the TEXTOR-94 tokamak [25, 26]. The combined discharge improved the reliability of IC antenna operation in the plasma production regime for wall conditioning. And it can be a promising method to reach a high RF wall conditioning efficiency [25, 26]. To date, there is no complete physics picture of the combined ECR + RF discharges. Nevertheless, it is noted that both techniques are complementary, and combining them may eliminate their individual disadvantages. For example, a disadvantage of ECR discharges is lower ion energy (<50 eV) than in IC discharges and a higher electron temperature (10–20 eV) [12].

This paper presents the first results of studying of the helium ECR plasma parameters and combined ECR + RF discharges in the TOMAS plasma facility by using a newly installed movable triple Langmuir probe system [27]. The main goal was to compare the density and electron temperature in ECR and ECR + RF discharges.

## 2. Experimental setup and diagnostic

### 2.1 Experimental setup

Experiments were performed in the TOMAS (TOroidal MAGnetized System) device [27, 28]. The scheme of the experimental setup is depicted in Figure 1. The vacuum chamber is a quasi - toroidal vessel with a minor radius of 0.26 m and a major radius of 0.78 m. The volume of the chamber is  $\sim 1.1 \text{ m}^3$ . The vacuum chamber was evacuated by turbo-molecular pump Pfeiffer TPU 1201PC (volume flow rate for  $\text{N}_2$  of 1250 l/s) in series with a rotary vane pump Pfeiffer DUO 35 (pumping speed of 8.889 l/s). The pressure was measured by a capacitance gauge (baratron) Pfeiffer CMR 375 (the pressure range of  $1.1 \times 10^{-1} - 1 \times 10^{-5}$  mbar) and the cold cathode gauge (penning gauge) Pfeiffer IKR 270 (the pressure range of  $1 \times 10^{-3} - 1 \times 10^{-9}$  mbar). The working gas was injected (see fig. 1) into the vacuum chamber using mass flow controller Bronkhorst F-201CV-200-VGD-88-V (flow rate of 4 – 200 sccm) calibrated for helium. The toroidal magnetic field is generated by a magnetic system consisting of 16 water-cooled coils. The magnetic system was powered by a DC power supply with the maximum output current of 2.2 kA, delivering a magnetic field on-axis up to 0.125 T. The value of the magnetic field is proportional to the coil current  $I_c$  [27]. The accuracy of the power supply current control is  $\sim 1 \%$ . Control and monitoring of systems TOMAS device (pumping, gas injection, magnetic field) is carried out using an integrated control system based on Siemens SIMATIC S7-1516-3 PN/DP controllers.

The microwave heating system consists of a 2.45 GHz microwave generator MUEGGE MH6000-213BF with water-cooled magnetron head, the magnetron power supply MUEGGE MW-PPEE3327-6K-016, a power monitoring and oscillator protection circuit, impedance matching circuit. The output flange of the magnetron is connected to a WR 340 waveguide. The transition element MUEGGE MW5002B-120YD is installed as an adapter from the rectangular waveguide to a circular port with a diameter of 100 mm. The transition element converts the  $\text{TE}_{10}$  mode in the rectangular waveguide to a  $\text{TE}_{11}$  mode propagating in the circular part. Microwave power is transmitted to the vacuum volume through a quartz window (see fig. 1) with a thickness of 6.22 mm and a diameter of 100 mm. The output microwave power of the generator is 0.6 – 6 kW. The generator can operate in a steady-state or pulsed regime with a pulse length down to 1 s.

The RF system was developed taking into account the geometric and technical features of the TOMAS device [29]. The RF system includes a generator, an amplifier, a transmission line, a matching circuit, an antenna, as well as control and diagnostic systems. It should be mentioned that the RF system can only be operated in a pulse regime. The current installation allows to have up to 4 s of pulse length. The RF generator Tektronix AFG 3252 (Arbitrary/Function Generator, frequency up to 120 MHz) operates at fixed frequency or frequency sweeps with sweep time from 1 ms to

300 s. The RF signal is amplified by a BONN Elektronik BLWA 0105-6000P solid-state amplifier in the frequency range of 10 – 50 MHz. The maximum CW output power is 6 kW. At the amplifier output, the power of the forward and reflected waves are measured with a directional coupler BONN Elektronik BDC 0105-70/10000 using high-speed Logarithmic Detector Power Meters (AD8310 0.1 – 440 MHz). High-frequency power from the amplifier is delivered to the antenna by the coaxial feeder line 50  $\Omega$  1 5/8". The RF antenna consisting of a single strap in an antenna box, is 3D-printed in Inconel 718 and, then, coated by a thin layer of copper with a thickness of 0.2 – 0.3 mm. The strap width is 90 mm with a thickness of 5 mm. The inner width of the antenna box is 180 mm. The shape of the antenna box repeats the circular curvature of the inner wall of the vacuum vessel at the low magnetic field side. The impedance matching system includes a pre-matching capacitor connected to the top of the antenna strap and a classical L-section matching circuit connected to the center of the strap. The RF and microwave systems are run by Python scripts.

The Data Acquisition System (DAS) of TOMAS (microwave and RF systems, pressure, plasma diagnostic systems) has 16 channels. The DAS is based on high precision signal conditioning amplifiers DEWETRON DAQP-V (bandwidth of 50 kHz, the input range of  $\pm 50$  V) with dynamic isolation which is connected to a National Instruments NI PXI-1042Q controller (two terminal blocks TB-2709). The Data Acquisition System is operated by LabView scripts. In more, the technical details of the TOMAS device are described in [27].

## 2.2 Langmuir probe diagnostic

The triple probe method was used to measure plasma parameters, such as the electron density and temperature, and their radial distributions along the diameter of the vacuum vessel. The triple probe technique [30-33] (proposed in 1965 [30]) has found applications in various plasma devices such as high-power impulse magnetron sputtering [34], theta-pinch [35], plasma accelerator [36], RF discharge [37, 38], tokamaks [39-41], and others systems [42-46]. To measure plasma parameters with a triple probe, a fairly simple measuring circuit is required. And the processing of experimental data is straightforward. The simplicity of measurements and data processing is the main advantage of this method. In addition, in the case of RF discharge, RF compensation of the triple probe is not required. As the system of three probes floats with the plasma following the plasma potential. A triple probe, like a double probe, can in principle respond to RF fields and provide internal RF

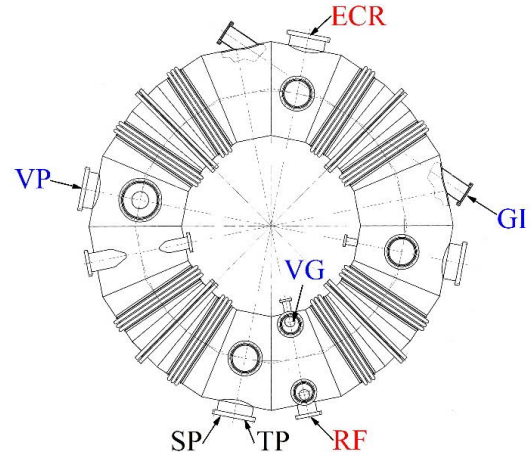


**Figure 1.** Scheme of the TOMAS device vacuum vessel. RF – RF antenna strap, ECR – microwave power input, GI – Gas Injection, VG – Vacuum Gauges, VP – Vacuum Pumping, SP – Single Probe, TP – Triple Probe.

compensation. The issue of RF compensation for a double probe is considered in detail in [47]. The results of measurements with a triple probe have been repeatedly compared with the results of a single [30, 38, 41] and double [37, 38, 41] Langmuir probes, as well as with the average density measured by a microwave interferometer [44]. Depending on the experimental conditions, the measurement error with a triple probe can range from several percent [37] to tens of percent [30, 37, 38, 44]. In paper [41], a difference between the data of the triple probe and other probes of the order of a factor of two was observed. This difference in the data is explained by the nonlinear distribution of the plasma parameter profile along the divertor targets. In fact, the triple probe method is a trade-off between simplicity and measurement accuracy, which is justified in many cases.

The movable symmetrical triple probe (see Fig. 2a) was designed, manufactured, and installed on the horizontal port of the vacuum vessel (see Fig. 1). It consists of a stainless steel holder (inner  $\phi$  9 mm) which embodies three probe tips insulated by cylindrical ceramic covers ( $\phi$  2.6 mm) enclosed in stainless steel thin pipes (outer  $\phi$  4 mm). The tips of the triple probe with a length of 4 mm are made of a tungsten cylindrical wire with a diameter of 0.8 mm. The tips are located equidistantly with a separation of 3.5 mm between each pair of tips. The triple probe is installed inside the 34 mm-diameter shaft of the vacuum manipulator which is equipped with an automated linear drive. The tips of the probes are connected via coaxial cables to the measuring electrical circuit (see Fig. 2b). The circuit is similar to that proposed in [30]. Accordingly, the triple probe worked in voltage mode (direct-display method). This mode uses two floating probes that are biased relative to each other (floating double probe system) and one probe floating independent. In this case, all three probe tips are at a floating potential. In the experiments, the voltage across the batteries was

$U_b = 57.2$  V, the resistance of the resistor was  $R = 984 \Omega$ . Circuit outputs are connected via coaxial cables to the DAS of TOMAS (see subsection 2.1). Accordingly, the signals  $U_1$  and  $U_2$  from the measurement circuit were fed to the DEWETRON DAQP-V and recorded by the PXI-1042Q. The relation of the measured voltage  $U_1$  and the  $T_e$  electron temperature is then [30]:

$$\frac{1 - \exp\left(-\frac{e_0 U_1}{k T_e}\right)}{1 - \exp\left(-\frac{e_0 U_b}{k T_e}\right)} = \frac{1}{2}, \quad (1)$$

where  $e_0$  is the charge of an electron, in C;  $k$  is the Boltzmann constant;  $U_1$  is voltage between tips 3 and 2 triple probe, in V;  $U_b$  is the bias voltage of the 2 pins tips 2 and 1 triple probe, in V;  $T_e$  is the electron temperature, in K. Having the knowledge of electron temperature, the plasma density is calculated using the following equation [30]:

$$N_e = \frac{(m_i)^{1/2} \times I \times \exp(1/2)}{S \times e_0 \times (k T_e)^{1/2} \times \left[ \exp\left(\frac{e_0 U_1}{k T_e}\right) - 1 \right]}, \quad (2)$$

where  $m_i$  is the ion mass, in kg;  $S$  is the surface area of the probe, in  $m^2$ ;  $I$  is the ion saturation current, in A. The ion saturation current is determined from the ratio  $I = U_2 / R$ , where  $U_2$  is the voltage drop across the resistor, in V;  $R$  is the resistance of a resistor, in  $\Omega$ ;  $N_e$  is plasma density, in  $m^{-3}$ .

The second movable probe is a single Langmuir Probe manufactured by Impedans Ltd. It is installed on the same horizontal port of the vacuum vessel as the triple probe (see fig. 1). The distance between the single and triple probes axes is 138 mm at the low magnetic field side. The tip of the probe is made of tungsten and has the shape of a circular cylinder with a height of 1.4 mm high, the end of which is in the form of a hemisphere with a diameter of 1.5 mm. The probe uses RF and DC compensation schemes. The range of plasma parameters measured by the probe is as follows: the floating potential between -145 V and 145 V, the plasma potential is between -100 V and 145 V, plasma density are ranging from  $1 \cdot 10^{10}$  to  $1 \cdot 10^{18} m^{-3}$ , the electron temperature is between 1 and 20 eV.

The triple probe was first tested in hydrogen and helium ECR plasma discharges at different parameters. A comparison was made for the plasma parameters measured by a triple probe and a single probe (see table 1) at two radial positions. As shown in Table 1, depending on the discharge parameters, the differences in temperature measurements of the probes are from -31.6 % to +4 %, and in terms of density from -30 % to +66.7 %. Since the probes measure the local plasma parameters, the differences in the probe measurements may partially be associated with plasma inhomogeneity in the torus, and with a positioning error in

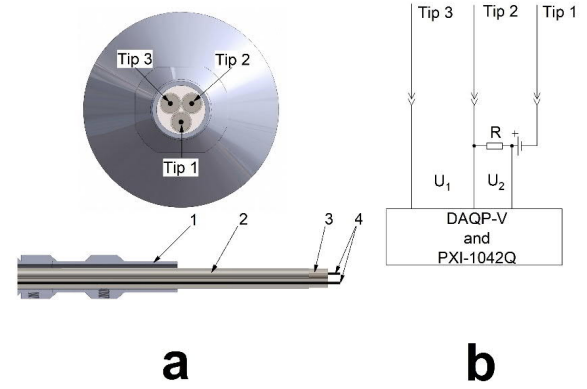


**Figure 2.** Sketch of the triple probe (a) and its connection circuit (b). 1 – probe holder, 2 – stainless steel thin pipe, 3 – ceramic cover, 4 – tips of the triple probe.

the installation of probes along the radial coordinate. The latter leads to the possibility that the probes are in the area of different magnetic field lines. On the other hand, the obtained differences in probe measurements are close to those obtained in [30, 37, 38, 44]. The results of these experiments show a satisfactory agreement between plasma parameter measurements by both probes.

### 2.3 Experimental details

The vacuum chamber was pumped down to a pressure of  $1.2 \cdot 10^{-5}$  Pa. Then the working gas - high purity He (99.996 % in gas bottle) - was continuously puffed in. The magnetic field at the center of the vacuum chamber was  $B(0) \approx 0.08$  T at a current in the coils  $I_c = 1.4$  kA. The condition for the fundamental ECR is the equality of the cyclotron frequency of rotation of an electron in a magnetic field:

$$\omega_{ce} = \frac{e_0 \times B}{m_e}, \quad (3)$$

where  $m_e$  is the electron mass,  $B$  is the magnetic induction, and the frequency of the electromagnetic wave  $\omega_{MW} = 2\pi \times f_{MW}$  [1,7,9]. Accordingly, for a microwave generator frequency  $f_{MW} = 2.45$  GHz, the condition  $\omega_{ce} = \omega_{MW} = 2\pi \times f_{MW}$  is satisfied at a magnetic field strength  $B = 0.0876$  T. At a current  $I_c = 1.4$  kA, the value  $B = 0.0876$  T corresponds to the radial coordinate  $r \approx -6.9$  cm (minus corresponds to the high field side region). In the experiments, the frequency  $f_{RF}$  of the RF generator was 25 MHz. In this case of a low magnetic field, the condition for fundamental IC resonance  $\omega_{ci} = \omega_{RF} = 2\pi \times f_{RF}$ :

$$\omega_{ci} = \frac{Z \times e_0 \times B}{m_i}, \quad (4)$$

where  $Z$  is the ion charge state for helium and hydrogen (hydrogen can be present in the discharge as a residual minority in the vacuum system) ions is not satisfied.

Table 1. Comparison of electron temperature and density ECR discharge measurement using single probe (SP) and triple probe (TP).

Initial parameters					$T_e$ , eV			$N_e$ , $10^{16} \text{ m}^{-3}$		$\delta^*$ , %
Gas	$p_0$ , Pa	$I_{\text{coil}}$ , A	$r$ , cm	$P_{\text{ECR}}$ , W	SP	TP	$\gamma^*$ , %	SP	TP	
H <sub>2</sub>	$7 \times 10^{-2}$	1200	4.28	1000	5	5.2	4	1.8	3	66.7
H <sub>2</sub>	$7 \times 10^{-2}$	1425	4.28	1000	1.9	1.3	-31.6	2.1	2.8	33.3
He	$4.3 \times 10^{-2}$	1400	16	804	11.9	9.1	-23.5	11	7.7	-30
He	$1.04 \times 10^{-1}$	1400	16	674	9.1	9.3	2.2	7.7	6.1	-20.8

$$\gamma^* = (T_{\text{TP}}/T_{\text{SP}} - 100) \cdot 100; \delta^* = (N_{\text{TP}}/N_{\text{SP}} - 100) \cdot 100$$

However, a regime of high cyclotron harmonics (HCH)  $\omega_{\text{RF}} = n\omega_{\text{ci}}$  ( $n$  number harmonic) is possible [27, 29, 48]. With the values of  $B$  and  $f_{\text{RF}}$  of these experiments, the HCH mode can be for H<sup>+</sup> ( $n > 13$ ), He<sup>2+</sup> ( $n > 27$ ) and He<sup>+</sup> ( $n > 54$ ).

The density and temperature of electrons was measured by a triple probe. The radial distributions of electron temperature and density are measured using a pulse-by-pulse technique. Five scans were carried out along the radius of the chamber at various values of pressure (see Table 2), microwave and RF power.

### 3. Results and discussion

#### 3.1 Overview experiments

The experiment scenario was as follows. At the first stage, with a duration of  $\sim 2$  s, the plasma was created and maintained by an ECR discharge. At the second stage (duration  $\sim 2$  s), RF power was additionally introduced into the plasma of the ECR discharge. Thus, a combined ECR + RF discharge was realized. A typical time evolution of plasma parameters, power, and pressure is shown in Figure 3.

For the ECR discharge, several stages can be conventionally distinguished (see Fig. 3). The first stage is microwave breakdown of the neutral gas and the creation of a preliminary plasma, visible in the temperature response of the probe, while the plasma density is well below  $< 1 \times 10^{16} \text{ m}^{-3}$ . In the second stage an increase of the plasma density (time duration  $\sim 0.7$  s) coincides with an increasing output power of the magnetron. The temporal and radial characteristics of electron temperature shown in Fig. 4a. indicate that the maximum value of  $T_e$  along the radius changes with time. At the initial moment, the maximum value of  $T_e$  is observed in the region of  $r \approx$  from -7.8 cm to -5.8 cm, which corresponds to the ECR region. Accordingly, in this area, the main electron heating mechanism is ECR. It is noted that the low absorption causes multiple reflections of the microwave in the vessel. It leads to multi-pass absorption and a microwave propagation and polarization mixture [27,28]. Further in time, the maximum  $T_e$  value shifts along the radius towards the low field side. Since the plasma density increases (see Fig. 4b), it is further possible to fulfill the conditions of the upper hybrid resonance (UHR) [9]:

$$\omega_{pe} = [(\omega_{MW} + \omega_{ce})(\omega_{MW} - \omega_{ce})]^{1/2}, \quad (5)$$

where  $\omega_{pe}$  electron plasma frequency:

$$\omega_{pe}^2 = \frac{e_0^2 \times N_e}{m_e \times \epsilon_0}, \quad (6)$$

where  $\epsilon_0$  is the electrical constant. Accordingly, the density value at which the UHR condition is satisfied can be expressed as:

$$N_e^{up} = \frac{(\omega_{MW}^2 - \omega_{ce}^2) \times m_e \times \epsilon_0}{e_0^2}. \quad (7)$$

The estimate shows that for the radial coordinate  $r = 0$  and  $r = 16$  cm, the UHR condition is satisfied at a plasma density  $N_e^{up}$  of  $\approx 1.3 \times 10^{16} \text{ m}^{-3}$  and  $3.2 \times 10^{16} \text{ m}^{-3}$ , respectively. At this stage, the microwave power  $P_{\text{ECR}}$  introduced into the plasma volume increases with time and reaches its maximum value (see Fig. 3c). The pressure in the vacuum chamber slightly increases from  $3.8 \times 10^{-2}$  Pa to  $\sim 4.2 \times 10^{-2}$  Pa (see Fig. 3e). Apparently, this is due to the plasma interaction with the vacuum vessel thus causing desorption of neutral atoms (molecules) from the wall. The third stage, the quasi-stationary regime, the plasma parameters change only slightly (see Fig. 3 and 4).

For the combined ECR + RF discharge, two stages may be distinguished. The first stage, the beginning of additional RF power input, with a duration of no more than 100 ms, when the transition to the quasi-stationary stage occurs (see Fig. 3 and 4). The second stage is the quasi-stationary regime.

To compare plasma parameters of ECR and ECR + RF discharges, two quasi-stationary time segments  $\Delta t_1$  and  $\Delta t_2$  were selected (see Fig. 3). The duration of each time section was 0.5 s. The average microwave and RF power is shown in Table 3. For each radial coordinate, the values of the plasma parameters were averaged over the respective time intervals. Next, the radial distribution of the electron density and temperature was constructed, as discussed in the next paragraph.

#### 3.2 ECR discharge

The measured radial distributions of density and temperature in the ECR discharge for three scans (S-1, S-2, S-3) are shown in Fig. 5. All three scans were carried out under almost the same conditions (see Tables 2 and 3). As it can be inferred from Fig. 5, high reproducibility of plasma



Table 2. Initial parameters when scanning (during the discharge the neutral pressure is balanced by discharge pumping and wall recycling).

Parameters	Scan number	
	S-1, S-2, S-3, S-4	S-5
Continuous Gas flow $Q$ (sccm)	35	20
Pressure $p_0$ in vacuum (Pa)	$3.8 \times 10^{-2}$	$2.7 \times 10^{-2}$
Number of neutral particles, $N_0$ ( $\text{m}^{-3}$ )	$9.96 \times 10^{18}$	$7.07 \times 10^{18}$

Table 3. Average data of microwave power ECR and RF power  $P_{\text{RF}}$  at two time intervals (see Fig. 3).

Scan number	$\Delta t_1$	$\Delta t_2$	
	$P_{\text{ECR}}$ , W	$P_{\text{ECR}}$ , W	$P_{\text{RF}}$ , W
S-1	$1039 \pm 31$	$996 \pm 30$	$86 \pm 2$
S-2	$1033 \pm 33$	$1015 \pm 28$	$243 \pm 4$
S-3	$1034 \pm 33$	$1035 \pm 23$	$649 \pm 13$
S-4	$2036 \pm 17$	$1851 \pm 18$	$725 \pm 7$
S-5	$1980 \pm 21$	$1924 \pm 29$	$689 \pm 9$

parameters from pulse to pulse is observed. A similar distribution of the density (see Fig. 5b) along the radius was observed earlier in [49-51]. The maximum electron temperature and density values respectively were 8.8 eV and  $1 \times 10^{17} \text{ m}^{-3}$ . The plasma pressure ( $N_e T_e$  the electron pressure) is in the range  $\approx (1.3 - 7.6) \times 10^{17} \text{ m}^{-3} \text{ eV}$  (see Fig. 6c, S-3). The degree of plasma ionization  $\alpha = N_e / (N_e + N_0)$  can be estimated from with the values of the plasma density from Fig. 5b and the density of neutral particles from table 2. For the estimation, we assume that the concentration of neutral particles (see table 2) does not change along the radius. In this case, the value  $\alpha$  along the radius is in the range  $1.6 \times 10^{-3} - 0.01$ . Hence, the degree of plasma ionization is not more than 0.01. In fact, a low-temperature and weakly ionized plasma is created in the ECR discharge.

The cut-off condition  $\omega_{\text{pe}} = \omega_{\text{MW}}$  for an O-wave when it propagates across the plasma column (perpendicular to the magnetic field) [9] is satisfied when the critical density

$$N_{ec} = \frac{\omega_{\text{MW}}^2 \times m_e \times \epsilon_0}{e_0^2} \quad (8)$$

is reached. Accordingly, for a frequency of 2.45-GHz, value  $N_{ec} = 7.45 \times 10^{16} \text{ m}^{-3}$ . As can be seen from Fig. 5b, the experimentally achieved maximum plasma density is higher than  $N_{ec}$ . At a concentration of electrons greater than the critical value,  $N_e > N_{ec}$ , the wave rapidly decays in the plasma. But the O-wave may penetrate the plasma a few centimeters deep (a consequence of their long wavelength  $\lambda_0 = 12.2 \text{ cm}$ ,  $\lambda_0$  vacuum wavelength) and be reflected, which partly leads to plasma heating or mode conversion. For the left-hand polarized (L) wave cut-off condition [9] is:

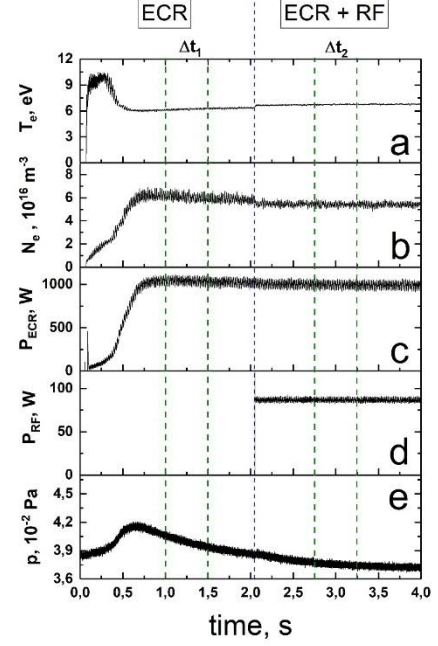


Figure 3. Time evolution of electron temperature  $T_e$  (a), electron density  $N_e$  (b), microwave power  $P_{\text{ECR}}$  (c), RF power  $P_{\text{RF}}$  (d), gas pressure (e) (gas – He, Scan number S-1, see Tables 2 and 3, radial position  $r = -5.8 \text{ cm}$ )

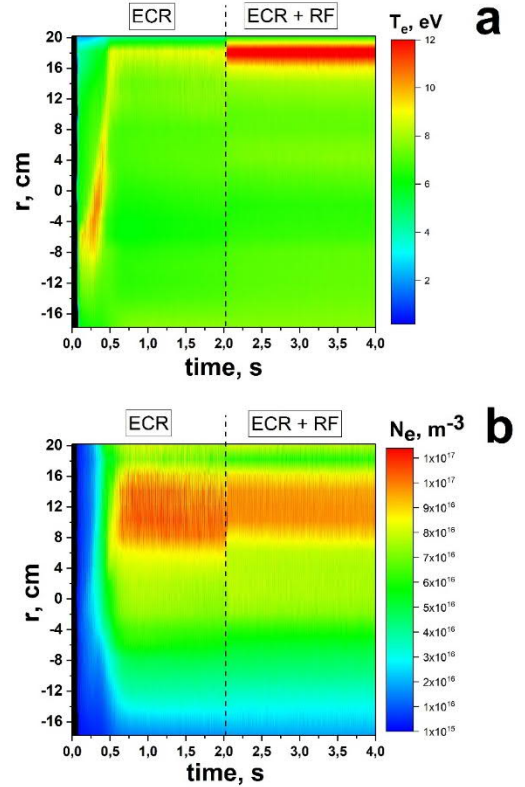
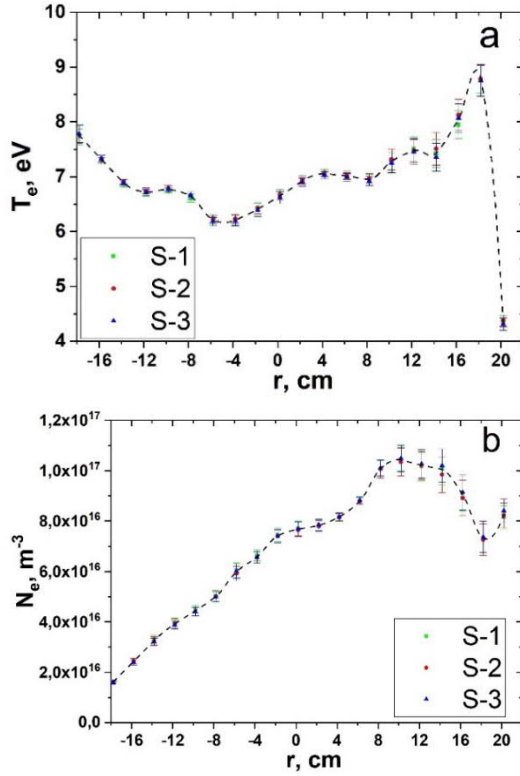


Figure 4. Time evolution of radial distribution electron temperature  $T_e$  (a) and density  $N_e$  (b) (gas – He, Scan number S-1, see Tables 2 and 3).



**Figure 5.** Radial distribution of electron temperature  $T_e$  (a) and density  $N_e$  (b) in ECR discharge (gas – He, S-1, S-2 and S-3 scan number, see Tables 2 and 3).

$$\omega_{pe} = \omega_{MW} \left( 1 + \frac{\omega_{ce}}{\omega_{MW}} \right)^{1/2}, \quad (9)$$

and the corresponding critical density is in the range  $1.28 - 1.6 \times 10^{17} \text{ m}^{-3}$ .

Comparison of the radial plasma parameters for two values of microwave power  $\sim 1 \text{ kW}$  (S-3) and  $\sim 2 \text{ kW}$  (S-4) is shown in Fig. 6. Other parameters, initial gas pressure and gas flow, are the same, see Table 2). As can be seen, an increase in the microwave power introduced into the discharge practically does not change the electron temperature. The density of plasma electrons increases by  $\sim 1.1 - 1.6$  times with increasing power (see fig. 6b, S-3 and S-4). The plasma pressure ( $N_e T_e$ ) at  $\sim 2 \text{ kW}$  (S-4) also increases in comparison to  $\sim 1 \text{ kW}$  (S-3) and is in the range of  $\approx 1.3 \times 10^{17} - 1 \times 10^{18} \text{ m}^{-3} \text{ eV}$  (see. Fig. 6c, S-4).

The measurements of radial plasma parameters also were carried out at a lower gas flow of 20 sccm and, respectively, the gas pressure of  $2.7 \times 10^{-2} \text{ Pa}$ , see Table 2, S-5. A comparison of results for S-4 and S-5 in Fig. 6 show clearly indicates that a decrease of the initial pressure leads to an electron temperature increase. The maximum temperature and density is  $\approx 13.1 \text{ eV}$  and  $n \approx 1.1 \times 10^{17} \text{ m}^{-3}$ , respectively. The plasma pressure ( $N_e T_e$ ) of the plasma at  $\sim 2 \text{ kW}$  (S-5) is in the range of  $\approx 3 \times 10^{17} - 1.1 \times 10^{18} \text{ m}^{-3} \text{ eV}$  (see Fig. 6c, S-5).

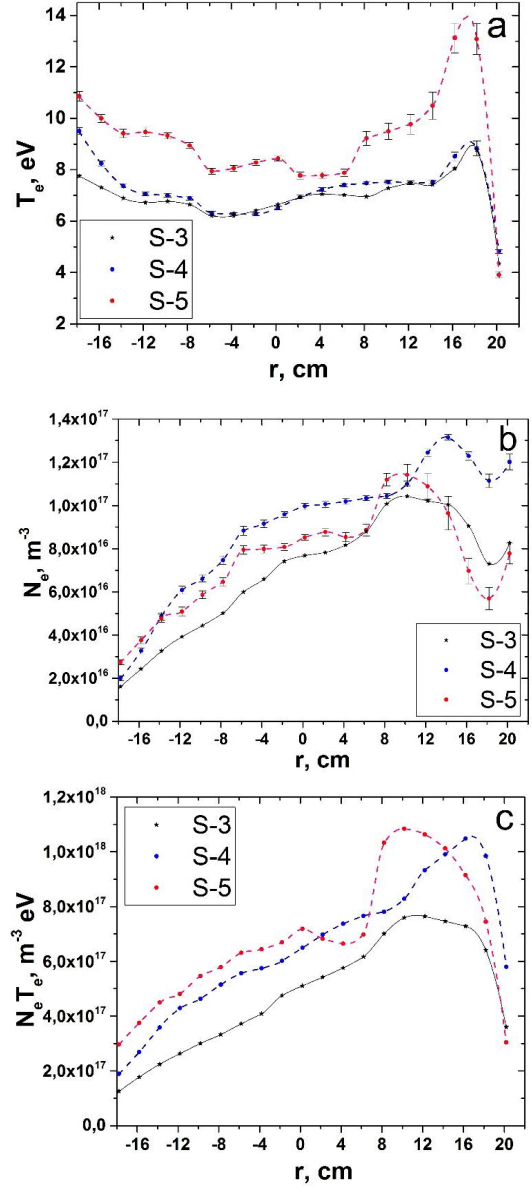


**Figure 6.** Radial distribution of electron temperature  $T_e$  (a), density  $N_e$  (b) and plasma pressure  $N_e T_e$  (c) in ECR discharge (gas – He, S-4, S-5 and S-3 scan number, see Tables 2 and 3).

The observed dependence of plasma parameters on pressure and power is characteristic for low-temperature weakly ionized plasma, including ECR discharge plasma [2,7]. In the case of a stationary plasma,  $T_e$  is dependent on the particle balance: production due to the ionization by electron impact, and their loss due to the diffusion. It does not depend, however, on the power [2]. In this case, a decrease in pressure should lead to the temperature increase, as it is indeed observed in the experiment (Fig. 6a S-4 and S-5). The plasma density at a constant pressure is determined by the balance of the absorbed power [2]. An increase of the absorbed power leads to an increase of the density, while  $T_e$  does not change, which is also observed in the experiment

(fig. 6a, b S-3, and S-4). In the case of a pressure change at the constant power,  $N_e$  changes because  $T_e$  changes with pressure. A decrease of pressure leads to an increase of  $T_e$  and a decrease of density, and this is observed experimentally (Fig. 6b S-4 and S-5). As it can be seen, the experimental results are qualitatively in a satisfactory agreement with the earlier results of ECR discharge studies [2,7]. The discussed cases lead to global changes in plasma parameters. However, these changes can lead to a redistribution of the absorbed power in the plasma volume. As a result, in some areas local changes in  $T_e$  and  $N_e$  may differ from the global changes. In this case, a more detailed analysis of the propagation and absorption of waves in plasma with specified parameters is required. The latter, however, is beyond the scope of this work.

### 3.3 Combined ECR+RF discharge

The radial distributions of density and temperature of the combined ECR + RF discharge are shown in Fig. 7. For comparison as well the averaged values of  $T_e$  and  $N_e$  are presented for the ECR-only phase of the 3 scans S-1, S-2, S-3. As it can be seen from Fig. 7a, the input of additional RF power into the ECR discharge leads to an increase of the electron temperature. For all three scans, in the region  $r \approx 4.2 - 18.2$  cm. the density is lower than for ECR discharge. The decrease in plasma density seems to be due to an increase in particles losses by diffusion. Comparison of the plasma pressure for the combined ECR + RF discharge shows that in the region  $r \approx 14.2 - 20.2$  cm, an increase in the plasma pressure of the combined ECR + RF discharge plasma with an increase of the input RF power is (see Fig. 7c).

For the frequency  $f_{RF} = 25$  MHz used in these experiments, the wavelength in vacuum is  $\lambda_0 = 11.99$  m, the wave vector in a vacuum is  $k_0 = 0.524 \text{ m}^{-1}$  ( $k_0^2 = (\omega_{RF}/c)^2$  with  $c$  is the speed of light in a vacuum). Waves do not propagate in a vacuum for a toroidal chamber in the case  $k_r^2 < 0$  [52]. The radial wave vector component is determined from the ratio [53]:

$$k_r^2 = k_0^2 - k_z^2 - k_\theta^2, \quad (10)$$

with  $k_z$  and  $k_\theta$  are the toroidal and poloidal wave vectors components respectively. The  $k_z$  and  $k_\theta$  values are determined by  $R_0$  major and  $r_0$  minor radii of the torus,  $n$  and  $m$  are toroidal and poloidal mode numbers, respectively  $k_z = n/R_0$  and  $k_\theta = m/r_0$ . In this case, the condition  $k_r^2 < 0$  is satisfied and the waves do not propagate in vacuum, which is typical for the most of small- or medium-size fusion machines [53]. For high-frequency discharges, it is essential that waves propagate in vacuum vessel installations and that they damp on plasma electrons. The absorption of RF power by electrons ensures their heating. In a low magnetic field, fast and slow waves can propagate in a small plasma column [15-17]. For a slow wave (SW), the excitation threshold at

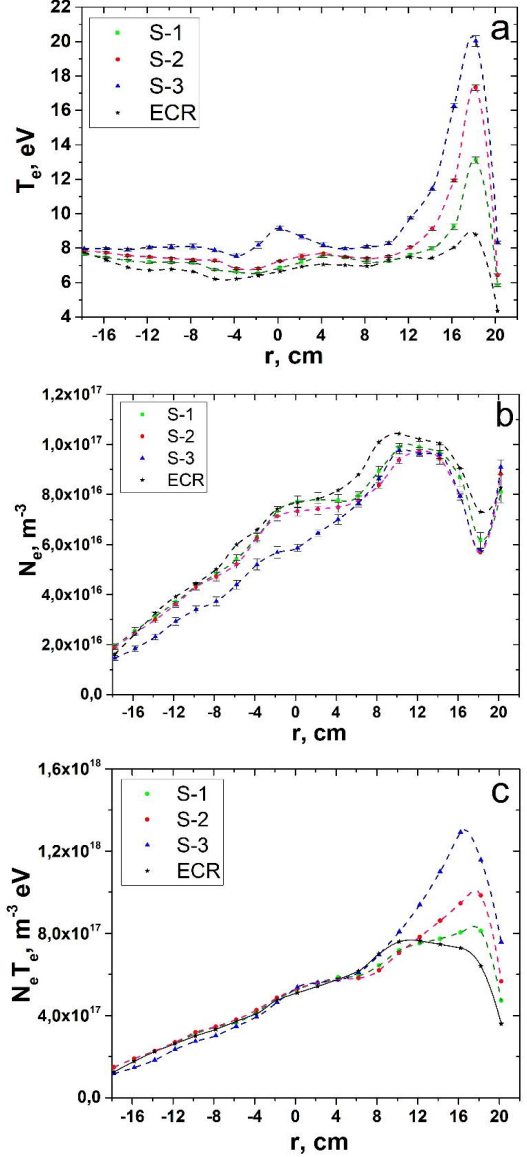


**Figure 7.** Radial distribution of electron temperature  $T_e$  (a), density  $N_e$  (b) and plasma pressure  $N_e T_e$  (c) in combined ECR + RF discharge (gas – He, S-1, S-2 and S-3 scan number; ECR – average values for ECR discharge scan S-1, S-2 and S-3, see Tables 2 and 3).

$|N_{||}| > 1$  ( $N_{||}$  parallel refractive index,  $N_{||} = k_{||} / k_0$ ) is determined by the cutoff SW at  $k_{\perp, SW} = 0$  ( $N_{\perp} = k_{\perp} / k_0$ ,  $k_{\perp}$  perpendicular refractive index) [53]. The minimum critical density above which SW can propagate is determined from the relation [53]:

$$\omega_{RF}^2 = \omega_{pe}^2 + \omega_{pi}^2, \quad (11)$$

where  $\omega_{pi}$  is the ion-plasma frequency. The estimate shows that the critical density for SW, in this case, is  $N_{ec}^{(1)SW} \approx 7.75 \times 10^{12} \text{ m}^{-3}$ . The upper limit of plasma density above which SW do not propagate for cold plasma is determined by the condition of lower hybrid resonance,  $k_{\perp, SW}^2 \rightarrow \infty$  [53]:



$$\omega_{\text{RF}}^2 = \omega_{\text{LH}}^2. \quad (12)$$

This condition is implemented, for the maximum value magnetic field on the high field side, at density  $N_{\text{ec}}^{(2)\text{SW}} \approx 9.6 \times 10^{16} \text{ m}^{-3}$ . In the region of a low field side,  $N_{\text{ec}}^{(2)\text{SW}} > 1 \times 10^{20} \text{ m}^{-3}$  and is significantly higher than the density obtained in the experiment. Accordingly, under these conditions, SW propagates in the plasma volume. For a fast wave (FW), the plasma density threshold is determined by the cutoff FW at  $k_{\perp, \text{FW}} = 0$ . The critical density for FW (for  $|N_{\parallel}| > 1$ ) can be estimated from the relation [53]:

$$\omega_{\text{pi}}^2 = (N_{\parallel}^2 - 1)\omega_{\text{ci}}(\omega_{\text{RF}} + \omega_{\text{ci}}). \quad (13)$$

As can be seen, the critical density also depends on  $k_{\parallel}$ , in contrast to SW. For a single strap antenna,  $k_{\parallel}$  can be estimated from the relation  $k_{\parallel} \sim \pi/w$  with  $w$  the antenna width [53]. For the TOMAS antenna, the estimate gives a value of  $k_{\parallel} \approx 34.91 \text{ m}^{-1}$ . For one single strap antenna, the maximum is at  $k_{\parallel} \approx 0$ . In this case, depending on the magnitude of the magnetic field (high and low field side), the critical density is in the range  $N_{\text{ec}}^{\text{FW}}$  from  $2.3 \times 10^{18} \text{ m}^{-3}$  to  $4.7 \times 10^{18} \text{ m}^{-3}$ . With values,  $k_{\parallel} \leq 5 \text{ m}^{-1}$  critical density  $N_{\text{ec}}^{\text{FW}} \leq 4.7 \times 10^{16} \text{ m}^{-3}$  and respectively FW can be propagated at the density values obtained in the experiment. The damping of waves, respectively, their absorption is due to the collisions of electrons with ions and neutral atoms (molecules). For a weakly ionized plasma, the decay mechanism for electron-neutral collisions is the main one. In addition, it is possible to convert waves into the Ion Bernstein Wave and cyclotron absorption on ions [15]. In [48] it was shown that for the HCH mode the electrons absorb more than 90% of the incoming power via electron-neutral collisions for both the Fast Wave and the Ion Bernstein Wave. The HCH mode for TOMAS was discussed in [27, 29].

As can be perceived, the dependence of plasma parameters on the input RF power in the combined ECR + RF discharge (see Fig. 7) at a constant gas flow and  $P_{\text{ECR}} = \text{const}$  differs significantly from the analogous dependence for the ECR discharge (Fig. 6: S-3 and S-4). For ECR discharge, with an increase in power, an increase in the plasma density along the radius are characteristic. In this case, the electron temperature changes insignificantly. As a result,  $N_e T_e$  also increases (see Paragraph 3.2). In the case of a combined ECR + RF discharge, an increase of power leads to an increase of the electron temperature along the radius. The plasma density either decreases or does not change, and  $N_e T_e$  increases only in the region of a weak magnetic field. These differences can be associated with different physical processes and mechanisms that occur in ECR and combined ECR + RF discharge. These are different types of waves characteristic of ECR and RF. Therefore, their propagation and power absorption can occur in different areas of the discharge. The input of additional RF power into the ECR discharge can lead to a change of the electron energy distribution function, as well as to the heating of plasma ions.

Fast neutral atoms are observed in RF discharge TOMAS [54]. Accordingly, the comparison of the dependence of plasma parameters on  $P_{\text{RF}}$  combined ECR + RF discharge and  $P_{\text{ECR}}$  ECR discharge is not straightforward. Therefore, experiments were carried out with a combined ECR + RF discharge with an increased  $P_{\text{ECR}}$  value.

The plasma parameters at the input microwave power of up to  $\sim 1.9 \text{ kW}$  in the combined ECR + RF discharge are shown in Fig. 8. An increase of the microwave power input to the combined ECR + RF discharge (the initial gas pressure and gas flow are the same, see Table 2) leads, as for ECR discharge (Fig. 6: S-3 and S-4), to density increase and a slight change of electron temperature along the radius (Fig. 8: S-4). Plots in Fig. 9 provide a comparison of plasma parameters at  $r = 18.2 \text{ cm}$  for different RF power values. An increase of the input RF power leads to an increase of the electron temperature and the plasma pressure of the plasma. In this case, an increase of the injected ECR power at given RF power also leads to the  $T_e$  and  $N_e T_e$  increase.

A decrease in the initial pressure leads to an increase in the electron temperature (Fig. 8a: S-5). A similar relationship is observed for ECR discharge (Fig. 6a: S-5). However, the electron temperature for the combined ECR + RF discharge is higher than for the ECR discharge. For example, at  $r \approx 18.2 \text{ cm}$ , the electron temperature is  $\approx 13.1 \text{ eV}$  and  $\approx 41.2 \text{ eV}$  for ECR and combined ECR + RF discharges, respectively.

Note that for the combined ECR + RF discharge, several cases can be conditionally distinguished (except for the boundary cases, only ECR or only RF discharge). The first is when the influence of the additional power (microwave or RF) on plasma parameters of the main discharge is practically minimal. In the second case, physical mechanisms characteristic of either ECR or RF discharge determine the generation and sustaining the plasma, while the injection of additional power (microwave or RF) leads to significant changes in plasma parameters. In the third case both ECR and RF are essential to maintain plasma parameters. Switching off the additional power (microwave or RF) leads to global changes in plasma parameters and even discharge termination. The results obtained indicate that the second case is realized in the experiments described above. ECR discharge is the main one for creating and maintaining

plasma, and the input of additional RF power leads to changes of plasma parameters. Thus, by adding RF, it becomes possible to change the plasma parameters independently of the ECR discharge.

In low-temperature weakly ionized plasma, one of the main processes in the formation of ions (multiply charged species) is ionization by electron impact of atoms and ions. The contribution to ionization of photoionization processes and ionization by atomic particles (ions) can be neglected. Ionization by electron impact can pass through several

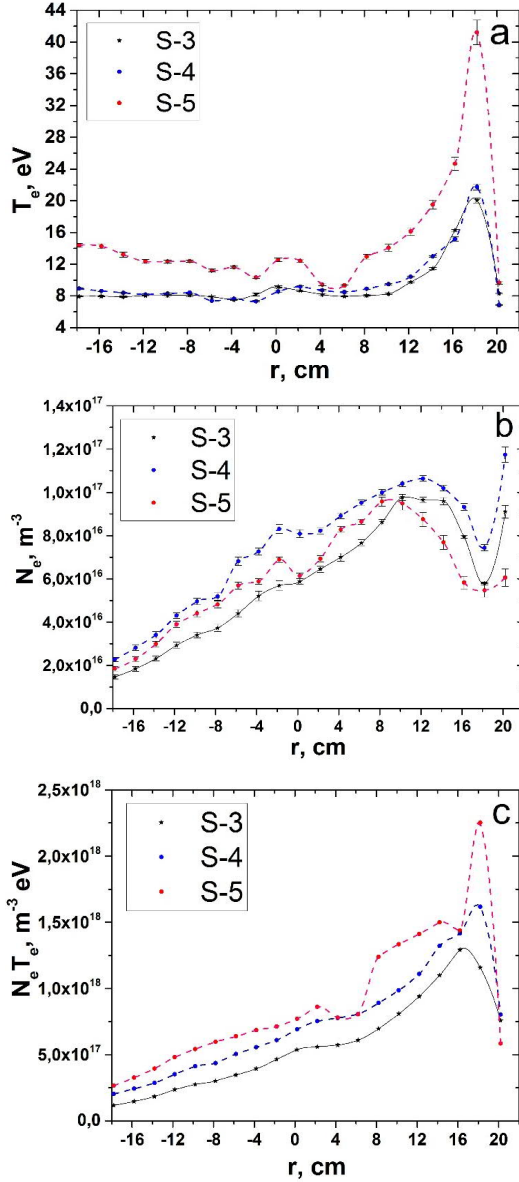


**Figure 8.** Radial distribution of electron temperature  $T_e$  (a), density  $N_e$  (b) and plasma pressure  $N_e T_e$  (c) in combined ECR+RF discharge (gas – He, S-4, S-5 and S-3 scan number, see Tables 2 and 3).

channels, namely, through the bound electron's direct transition to the continuum or the electron's cascade transitions to the continuum. Accordingly, the collision of an electron with an atom (ion) can lead to direct ionization, stepwise ionization, and autoionization [55]. Direct ionization can be either single-electron ionization ( $\text{He} + e \rightarrow \text{He}^+ + 2e$ ,  $\text{He}^+ + e \rightarrow \text{He}^{2+} + 2e$ ) or multiple-electron ionization ( $\text{He} + e \rightarrow \text{He}^{2+} + 3e$ ). The single ionization cross-section is greater than the multiple ionization cross-section. The formation of multiply charged ions occurs more

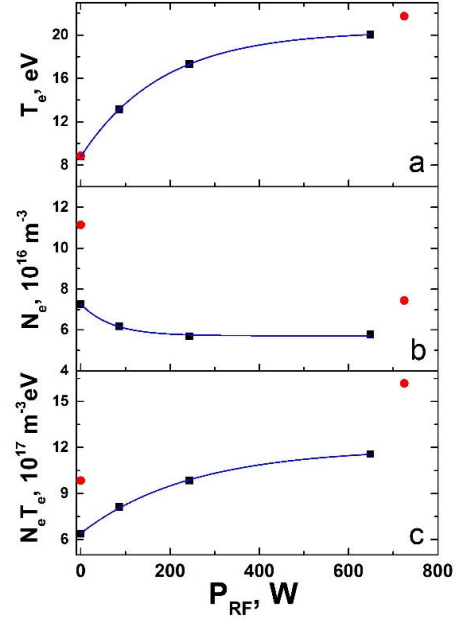


**Figure 9.** Temperature (a), electron density (b) and plasma pressure  $N_e T_e$  (c) versus RF power (gas – He). Black squares indicate  $P_{\text{ECR}} \approx 1000$  W, red circles correspond to  $P_{\text{ECR}} \approx 2000$  W. Radial position  $r = 18.2$  cm,  $p_0 = 3.8 \times 10^{-2}$  Pa.

efficiently in successive processes of single ionization of an atom (ion) [56]. Let us estimate the characteristic times of  $\text{He}^{2+}$  formation (ionization collision time)  $\tau_i = (N_{\text{He}^+} \langle \sigma v \rangle)^{-1}$ , where  $\langle \sigma v \rangle$  electron impact ionization rate, in the reaction  $\text{He}^+ + e \rightarrow \text{He}^{2+} + 2e$ , for ECR discharge and ECR + RF discharge taking into account the experimental data  $N_{\text{He}^+} \approx N_e$ . The  $\text{He}^+$  ionization cross-section was taken from [57]. The electron energy distribution function was assumed to be Maxwellian. The estimate shows that for ECR discharge the minimum time  $\tau_i$  is greater than the discharge time scans S-1 – S-4, i.e. more than 2 s, and for scan S-5  $\tau_i \approx 0.5$  s. Accordingly, under these conditions of ECR discharge, the probability of the formation of two charged ions is very small. For a combined ECR + RF discharge, the minimum time  $\tau_i \approx 0.37$  s,  $\approx 0.17$  s,  $\approx 0.16$  s for scans S-1, S-2, S-3, respectively. In this case, the probability of the formation of  $\text{He}^{2+}$  ions is higher than that under the ECR conditions. However, their density will be minimal. Times  $\tau_i$ , of combined ECR + RF discharges  $\approx 0.06$  s,  $\approx 0.02$  s for scans S-4, S-5, respectively. Estimation of the  $\text{He}^{2+}$  ion density for scan S-5 assuming stationary equilibrium gives value of  $\sim 10^{13} \text{ m}^{-3}$ . If there is a flux of fast electrons in the plasma, it will contribute to the overall balance of ions  $\text{He}^{2+}$ . That said the higher is the concentration of fast electrons, the greater will be their contribution to the balance of formation of  $\text{He}^{2+}$  ions.

The collision of excited atoms (molecules) in metastable state with neutral particles (in metastable state) can lead to

the formation of ions, for example, in the Penning process of ( $\text{He}^* + \text{He}^* \rightarrow \text{He} + \text{He}^+ + e$ ) or associative ( $\text{He}^* + \text{He}^* \rightarrow \text{He}_2^+ + e$ ) ionization [58–60]. Such processes can take place in weakly ionized plasma, and the rate constant of these processes is quite high  $\approx (2\text{--}4) \times 10^{-15} \text{ m}^3/\text{s}$  [59]. However, the contribution of these processes to the particle balance will be small. Since the characteristic diffusion time of a metastable particles under the conditions of these experiments is small  $\tau_D \approx 8 \times 10^{-5} \text{ s}$  ( $\tau_D = \Lambda^2/D$  where  $\Lambda$  is the characteristic diffusion length,  $D$  the diffusion coefficient of metastable atoms in the gas was taken from [60]).

#### 4. Concluding Remarks

This paper explores for the first time the parameters in helium ECR plasma and combined ECR + RF discharges in TOMAS. The conducted studies of the ECR discharge showed that in the investigated range of pressures and power, a weakly ionized low-temperature plasma is formed in the discharge. The experimentally observed dependences of plasma parameters on pressure and power are in qualitative agreement with the earlier results of ECR discharge studies and are characteristic of low-temperature weakly ionized plasma. The maximum electron temperature observed in the electron heated plasma is up to  $\approx 13.1 \text{ eV}$  and the plasma density is up to  $\approx 1.3 \times 10^{17} \text{ m}^{-3}$ , at the input microwave power of up to  $\approx 2 \text{ kW}$ . In the case of a combined ECR + RF discharge, the ECR discharge is the main one for creating and maintaining plasma, and the input of additional RF power leads to changes in plasma parameters. The maximum electron temperature observed in the combined plasmas is up to  $\approx 41.2 \text{ eV}$  at the input microwave power (2.45 GHz) of up to  $\sim 1.9 \text{ kW}$  and RF (25 MHz) power of up to  $\sim 0.7 \text{ kW}$ . Thus, by adding RF, it becomes possible to change the plasma parameters independently from the ECR discharge. In this case, a change in the frequency of the RF discharge and the magnetic field can lead to a change in the parameters of the combined ECR + RF discharge. Accordingly, this provides additional levers for controlling plasma parameters. This is of particular interest as it allows to adjust the fluxes and energy of particles that leave the plasma volume to approach conditions needed for surface interaction studies. These include aspects of wall conditioning techniques and fusion edge plasmas. The first experiments to determine the fluxes of low-energy neutral particles from hydrogen plasma were carried out at the TOMAS facility [61]. The flux of neutral atoms and their temperature was higher in the combined ECR + RF discharge than in the ECR [61]. In further studies is expected to investigate discharges in more detail to optimize conditions and develop a wall conditioning strategy. Finally, as many experimental thermonuclear fusion devices are equipped both with ECR and RF systems the combined discharge can be readily implemented on large devices.

#### Acknowledgements

This work has been carried out within the framework of the EUROfusion Consortium and has received funding from the Euratom research and training programme 2014–2018 and 2019–2020 under Grant Agreement No. 633053. The views and opinions expressed herein do not necessarily reflect those of the European Commission.

Authors are thankful to Dr. M. Rubel for his comments.

#### ORCID iDs

Yu V Kovtun <https://orcid.org/0000-0003-4948-0896>  
 T Wauters <https://orcid.org/0000-0002-2941-7817>  
 A Gorlaev <https://orcid.org/0000-0002-2599-182X>  
 S Möller <https://orcid.org/0000-0002-7948-4305>  
 D López-Rodríguez <https://orcid.org/0000-0001-5246-4972>  
 K Crombé <https://orcid.org/0000-0001-9883-3972>  
 S Brezinsek <https://orcid.org/0000-0002-7213-3326>  
 A Dinklage <https://orcid.org/0000-0002-5815-8463>  
 D Nicolai <https://orcid.org/0000-0003-1260-8796>  
 Ch Linsmeier <https://orcid.org/0000-0003-0404-7191>  
 J Buermans <https://orcid.org/0000-0001-5623-551X>  
 S Moon <https://orcid.org/0000-0002-0865-7387>  
 R Ragona <https://orcid.org/0000-0002-3225-5732>  
 P Petersson <https://orcid.org/0000-0002-9812-9296>

#### References

- [1] Ferreira C M and Moisan M (ed) 1993 *Microwave Discharges Fundamentals and Applications* (Springer Science+ Business Media, LLC)
- [2] Popov O A (ed) 1995 *High density plasma sources. Design, Physics and Performance*. (Noyes Publications).
- [3] Conrads H and Schmidt M 2000 *Plasma Sources Sci. Technol.* **9** 441
- [4] Chabert P and Braithwaite N St . 2011 *Physics of radio-frequency plasmas* (Cambridge university press)
- [5] Chen F F 2015 *Plasma Sources Sci. Technol.* **24** 014001.
- [6] Lebedev Yu A 2015 *Plasma Sources Sci. Technol.* **24** 053001
- [7] Asmussen J et al. 1997 *IEEE Trans. Plasma Sci.* **25** 1196
- [8] Lloyd B 1998 *Plasma Phys. Control. Fusion* **40** A119
- [9] Guest G 2009 *Electron cyclotron heating of plasmas* (WILEY-VCH Verlag GmbH & Co. KGaA.)
- [10] Wolf R C et al. 2019 *Plasma Phys. Control. Fusion* **61** 014037
- [11] Noterdaeme J.-M. 2020 *AIP Conf. Proc.* **2254** 020001
- [12] E de la Cal and Gauthier E 2005 *Plasma Phys. Control. Fusion* **47** 197
- [13] Douai D et al. 2011 *J. Nucl. Mater.* **415** S1021
- [14] Wauters T et al. 2020 *Plasma Phys. Control. Fusion* **62** 034002
- [15] Lozin A V et al. 2013 *Plasma Phys. Rep.* **39** 624
- [16] Moiseenko V E et al. 2014 *Nucl. Fusion* **54** 033009
- [17] Kovtun Yu V et al. 2020 *Acta Phys. Pol. A* **138** 632
- [18] Wauters T et al. 2018 *Nucl. Fusion* **58** 066013
- [19] Gorlaev A et al. 2019 *Nuclear Materials and Energy* **18** 227
- [20] Yaowei Yu et al. 2008 *Phys. Scr* **79** 015502

- [21] Misina M and Pokorny P 2003 *Surf. Coat. Technol.* **174–175** 914
- [22] Wang L et al. 2010 *Vacuum* **84** 348
- [23] Zhou H Y et al. 2010 *Rev. Sci. Instrum.* **81** 033501
- [24] Hala A M, Oksuz L and Ximing Zhu 2016 *Plasma Sci. Technol.* **18** 832
- [25] Lysssoivan A et al. 2001 *AIP Conf. Proc.* **595** 146
- [26] Gauthier E et al. 2001 *28 th EPS Conference on Controlled Fusion and Plasma Physics*, (June 18-22, 2001, Madeira) P5.094
- [27] Gorlaev A et al. 2021 *Rev. Sci. Instrum.* **92** 023506
- [28] Störk H B et al. 2001 *Fusion Sci. Technol.* **39** 54
- [29] Louche F et al. 2017 *Fusion Eng. Des.* **123** 317
- [30] Sin Li Chen and Sekiguchi T 1965 *J. Appl. Phys.* **36** 2363
- [31] Demidov V I et al. 2002 *Rev. Sci. Instrum.* **73** 3409
- [32] Lobbia R B and Beal B E 2017 *J. Propuls. Power* **33** 566
- [33] Benedikt J, Kersten H and Piel A 2021 *Plasma Sources Sci. Technol.* **30** 033001
- [34] Lockwood E F, Karkari S K and Bradley J W 2017 *J. Phys. D: Appl. Phys.* **50** 295201
- [35] Jung S et al. 2011 *J. Nucl. Mater.* **415** S993
- [36] Borthakur S et al. 2018 *Phys. Plasmas* **25** 013532
- [37] Naz M Y et al. 2011 *Prog. Electromagn. Res.* **114** 113
- [38] Ghosh S et al. 2014 *Plasma Sources Sci. Technol.* **24** 015017
- [39] Hernandez W A et al. 2019 *J. Plasma Phys.* **85** 905850407
- [40] Qayyum A et al. 2016 *J. Fusion Energy* **35** 205
- [41] Xu J C et al. 2019 *J. Instrum.* **14** 06028
- [42] Kumar A et al. 2009 *J. Appl. Phys.* **106** 043306
- [43] Lee S G and Bak J G 2001 *Rev. Sci. Instrum.* **72** 442
- [44] Mackel F et al. 2011 *Meas. Sci. Technol.* **22** 055705
- [45] Qayyum A et al. 2013 *Rev. Sci. Instrum.* **84** 123502
- [46] Roche T et al. 2014 *Rev. Sci. Instrum.* **85** 11D824
- [47] Caneses J F and Blackwell B 2015 *Plasma Sources Sci. Technol.* **24** 035024
- [48] Lysssoivan A et al. 2014 *AIP Conf. Proc.* **580** 287
- [49] Ihde J et al. 1999 *26 th EPS Conference on Controlled Fusion and Plasma Physics* (Maastricht, 14 - 18 June 1999) ECA **23J** 709.
- [50] Ihde J et al. 2001 *J. Nucl. Mater.* **290-293** 1180
- [51] Sugai H et al. 2001 *J. Plasma and Fusion Research* **77** 130
- [52] Lysssoivan A et al. 2012 *Plasma Phys. Control. Fusion* **54** 074014
- [53] Usoltceva M et al. 2019 *Plasma Phys. Control. Fusion* **61** 115011
- [54] Möller S et al. 2021 *24th International Conference on Plasma Surface Interaction in Fusion Devices (PSI-24)*
- [55] Itikawa Y (ed) 2000 *Landolt–Börnstein—Group I Elementary Particles, Nuclei and Atoms 17A (Interactions of Photons and Electrons with Atoms)* (Berlin: Springer)
- [56] Kovtun Yu V, Shapoval A N and Siusko Y V 2019 *Plasma Sources Sci. Technol.* **28** 105009
- [57] Mattioli M et al. 2007 *J. Phys. B: At. Mol. Opt. Phys.* **40** 3569
- [58] Kovtun Yu V et al. 2016 *Ukr. J. Phys.* **61** 702
- [59] Smirnov B. M. 2015 *Theory of Gas Discharge Plasma* (Berlin: Springer)
- [60] Smirnov B. M. 2008 *Reference Data on Atomic Physics and Atomic Processes* (Berlin: Springer)
- [61] Moon S et al. 2021 *Phys. Scr.* **96** 124025